IEEE TRANSACTIONS ON POWER ELECTRONICS, VOL. 39, NO. 4, APRIL 2024

High-Gain High-Frequency Three-Phase LLC Resonant Converter Design Based on the Wye–Delta Transformer for Aircraft Applications

Daniel Ríos Linares, *Student Member, IEEE*, Alberto Delgado Expósito, *Member, IEEE*,
and Miroslav Vasić, *Senior Member, IEEE*

***Abstract*—The requirements for small form-factor power supplies drive the need for high-frequency small magnetic components and high efficiency to obtain thermal stability. When combined with high output power, magnetic optimization becomes crucial in the pushing of the boundaries of magnetic shrinkage. Among those applications in need of power dense systems, aircraft is considered one of the most restrictive due to its ultrahigh reliability and miniaturization in both volume and mass. On-board equipment transfers the responsability to the power stage classifying it as mission-critical. The selection of a multiphase converter enables the desired magnetic components' shrinkage. With these objectives in mind, a three-phase LLC based on the wye–delta transformer is selected as a promising topology to fulfill high efficiency, small form factor, effective power density, and high voltage step-down in aircraft applications. The focus of this work is the listing of the guidelines on the design of three-phase magnetic components with the compensation of an asymmetric structure (EE/EI cores) to match its magnetic coupling. The multiple sources of power losses are analyzed and optimized, including high-amplitude high-frequency currents traveling around the printed circuit board. This article presents the design of a unidirectional dc–dc converter with an input voltage range of 235–285 V to 28 V at the output, controlled by a frequency range of 15% for a nominal output power of 1 kW reaching an efficiency of 96%.**

***Index Terms*—Coupled inductors, dc–dc converter, high frequency, high power density, high voltage step-down, LLC, magnetic optimization, three phase.**

NOMENCLATURE

LLC converter design

L_r	Resonant inductance.
C_r	Resonant capacitance.
L_μ	Magnetizing inductance.
Z_r	Characteristic impedance of the resonant tank.
Q	Quality factor of the resonant tank.
ω_r	Resonant angular frequency.
m	Total inductance to magnetizing ratio.

Circuit voltages and currents

k	Identifier of the phase ($k = A, B, C, a, b, c$).
$i_{L_r,k}$	Current through the resonant tank for phase k.
$v_{C_r,k}$	Voltage across the resonant capacitance for phase k.
V_I	Input voltage (DC).
V_O	Output voltage (DC).
$\bar{U}_k$	Voltage across the windings (phasor).
$\bar{I}_k$	Current through the windings (phasor).

Magnetic design

$\hat{B}$	Peak of the B-field within the core.
f_S	Switching frequency.
T_S	Switching period.
A_e	Effective cross-sectional area of the magnetics.
n_p	Number of turns of the transformer (primary).
n_s	Number of turns of the transformer (secondary).
n	Winding turns ratio of the transformer.

Eddy current power losses in a foil conductor

F_R	Correction factor for Eddy currents for foil conductor.
t	Thickness of the foil (copper track).
δ	Skin effect depth.
ν	Ratio between the skin depth and thickness.
μ_{Cu}	Absolute permeability of the copper.
ρ_{Cu}	Absolute resistivity of the copper.
$\hat{I}$	Peak of the current through the conductor.

I. INTRODUCTION

AIRCRAFT electronic applications introduce challenging conditions with an extensive regulatory basis . The half-brick format for power supplies constitutes a typical form factor in aircraft converters. This means that the converter is height constrained, reducing the available space for magnetic components. These volume and mass restrictions are correlated with the mandatory high efficiency, as heat dissipation is challenging. In addition, electromagnetic interference has to be under control as power converters should not perturbate the onboard apparatus

---

Manuscript received 1 June 2023; revised 11 September 2023 and 6 November 2023; accepted 2 December 2023. Date of publication 6 December 2023; date of current version 16 February 2024. Recommended for publication by Associate Editor C.-J. Chen. *(Corresponding authors: Daniel Ríos Linares; Alberto Delgado Expósito; Miroslav Vasić.)*

Daniel Ríos Linares is with the Departamento de Automatica, Ingenieria Electrica y Electronica e Informatica Industrial, Escuela Técnica Superior de Ingenieros Industriales, Universidad Politécnica de Madrid, 28006 Madrid, Spain (e-mail: d.rios@upm.es).

Alberto Delgado Expósito is with the Escuela Técnica Superior de Ingenieros Industriales, Universidad Politécnica de Madrid, 28006 Madrid, Spain (e-mail: a.delgado@upm.es).

Miroslav Vasić is with the Centro de Electronica Industrial, Universidad Politécnica de Madrid, 28006 Madrid, Spain (e-mail: miroslav.vasic@upm.es).

Color versions of one or more figures in this article are available at https://doi.org/10.1109/TPEL.2023.3339973.

Digital Object Identifier 10.1109/TPEL.2023.3339973

in mid-flight, establishing soft-switching topologies as a wise option and resonant converters as a promising choice.

LLC resonant converters possess all these features allowing the designer to increase the switching frequency due to its intrinsic zero-voltage switching (ZVS) on the entire load range allowing the shrinkage of magnetic components and, thus, increasing the power density. Contemporary gallium nitride (GaN) transistors with their low capacitance are the enablers of the high-frequency operation.

A very high voltage step-down dc–dc conversion is needed, as onboard equipment need 28 V dc to operate from a wide input voltage range (200–330 V) [1]. When developing high voltage gain in isolated converters, most of the conversion is achieved by the transformer winding ratio resulting into an overcrowded window for the magnetics as well as higher power losses due to proximity effects.

To solve it, single-stage converters are built upon multiple transformers to reduce current stresses [2], series–parallel multiwinding transformers can be employed [3], series converters are adopted [4], and matrix transformers are proposed [5]. Multistage solutions can also be found in the literature by interleaving LLC converters [6] or through series–parallel architecture [7]. Some scholars focus on the addition of other operating modes such as phase-shift modulation [8], multiple output [9], pulsewidth modulation (PWM), and amplitude modulation [10].

Moreover, due to high input and output current ripple, the effective power density at system level may be reduced as bigger filtering passive devices will have to be dimensioned.

These issues bring us to the implementation of a multiphase solution into the LLC converter family, as these topologies allow the designer to choose among different techniques to reduce the input and output current ripple [11], lessen the current per phase [12], or integrate magnetic components [13].

This multiphase concept can be applied at the inverter and rectifier, as in the three-phase LLC [14]. These ideas are still valid for center-tap rectification [15], full-bridge rectification [16], creating matrix transformers [11], or with interleaved structures within the three-phase configuration [12], [17].

Three-phase systems offer specific additional benefits, as three-phase inductors [18] and transformers [19] ensure the integration of magnetics down to two individual magnetic components. The arrangement of the windings of the transformer can be in wye–delta [19], delta–wye, delta–delta [15], and wye–wye [16]. The resonant capacitance arrangement into a delta configuration (Δ–C_r) [14] reduces the required individual value of capacitance. For all these reasons, the three-phase LLC converter is a promising candidate topology to be analyzed and optimized for high-power-density applications.

The need for a low-profile form-factor converter means that, due to the limited magnetic permeability of asymmetric magnetic cores, an electrical unbalance of these components becomes noticeable. This is not exclusive of the multiphase LLC converter but of any converter able to be configured in a multiphase manner such as the dual active bridge [20] and will be addressed in this research work with the compensation of magnetic coupling between the columns of an EE/EI magnetic core.

TABLE I
THREE-PHASE TRANSFORMERS' TURN RATIO FOR UNITY GAIN

Feature	Wye–Wye	Wye–Delta	Delta–Delta	Delta–Wye
Voltage gain	1	$\sqrt{3}$	1	$1/\sqrt{3}$
Turn ratio	$1:1$	$1/\sqrt{3}:1$	$1:1$	$\sqrt{3}:1$

TABLE II
SPECIFICATIONS FOR THE CONVERTER

Parameter	Value	Description	
V_I	270 V	Nominal	Input voltage
	235-285 V	Normal	
	220-325 V	Abnormal	
V_O	28 V	Nominal	Output voltage
	26.6-29.4 V	Range	
P_O	1 kW	Nominal	Output power
	0-1 kW	Range	
ΔF_x	15 %	Normal	Frequency range
	100-1000 W	In range	
V_{ins}	2250 V	Minimum	Insulation
w	61 mm	Width	Converter dimensions
l	58 mm	Length	
h	13 mm	Height	

The low profile of the converter makes it necessary to select a topology with inherent gain in order to minimize the number of turns required in the transformer and take full advantage of the topology. Three single-phase transformers can be connected into a single three-phase transformer, and among the different possible connections (wye, delta, zig-zag, etc.), as shown in Table I, the wye–delta transformer includes an intrinsic $\sqrt{3}$ step-down in the voltage conversion ratio (and a $\sqrt{3}$ step-up in the current) decreasing the voltage conversion ratio imposed on the winding turn ratio $n = n_p/n_s$ and helping further scaling of the LLC transformer.

This feature is crucial in this case as the specifications of the main line aircraft dc–dc converters have to step down the voltage from hundreds of volts to 28 V. In this article, a 270-to-28-V 1-kW 900-kHz three-phase LLC based on the wye–delta transformer is analyzed in detail.

This article presents a three-phase LLC dc–dc converter topology with a wye–delta transformer, a combination suitable to satisfy the high voltage gain required in aircraft applications. Insights on the operation of the topology will be exposed together with the design guidelines of the resonant tank to fulfill the strict operating frequency variation (10% around the nominal switching frequency) as well as the range of the input voltage and output power to regulate the output to 28 V (full specifications are shown in Table II). The geometry dimensioning of magnetic components will be proposed, eliminating the inherent asymmetry of three-port magnetic cores.

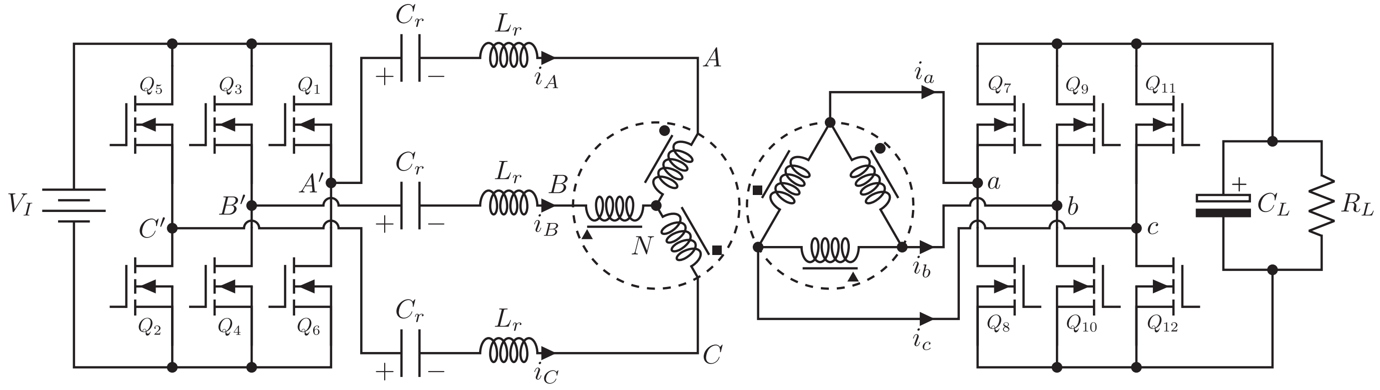

Fig. 1. Wye–delta three-phase LLC resonant converter.

The contributions of the research outlined in the present work are as follows.

1) *High-gain low-profile form factor:* Designing a converter in a low-profile form factor and for a wide input voltage range with frequency variation constraints is a key contribution for applications with restricted converter volume, such as avionics. The full design procedure is discussed: component selection, winding structure, practical application on the magnetics (transformer and inductor), analysis of power losses, and layout implications of the rectifier.
2) *High efficiency:* Emphasis on high efficiency is a significant contribution, especially in the context of aircraft applications where energy efficiency is critical for the overall system performance. Optimization of the converter in magnetics with flexibility in their design is considered, enabling their integration.
3) *Balanced magnetic structure:* The development of a balanced magnetic structure is crucial for the proper operation of the converter. This is achieved by producing an even magnetic flux distribution between columns (central and lateral columns while also maintaining among lateral columns). This balance is essential for optimal transformer performance in a three-phase LLC resonant converter contributing to reduced power losses, improved efficiency, and enhanced overall converter performance. The proposed technique is conceptualized, experimentally demonstrating its consequences.

The rest of this article is organized as follows. Section II describes the operating principle that governs the converter allowing the designer to meet the restrictions defined by the specifications: operating ranges of switching frequency, input voltage, and output power. The strict height limitation of 13-mm drives the design to a planar core constraining the core geometry and increasing the winding complexity. Section III exposes a novel model to achieve symmetric coupling for the planar transformer and inductor, identifying and compensating the effect of the fringing in the magnetic coupling design. In Section IV, Pareto optimization is developed for a constrained design space limited by technological limitations (materials), manufacturing process (core geometry), and application-specific features (converter maximum height). A demonstrator will be built in Section V, and the experimental results for 1 kW are given in Section VI. Finally, Section VII concludes this article.

II. THEORETICAL ANALYSIS

A. Operating Principle

The simplified schematic of the proposed three-phase LLC converter based on the wye–delta transformer is shown in Fig. 1. Both the inverter and the rectifier operate with three 50% duty cycle PWM signals (one for each leg) 120 ° apart.

The circuit behavior is completely defined once we have chosen the gate voltage at each and every one of the switches, and its steady state can be known.

The sum of currents for the three primaries and three secondaries null each other

$$i_A(t) + i_B(t) + i_C(t) = 0 \tag{1a}$$

$$i_a(t) + i_b(t) + i_c(t) = 0. \tag{1b}$$

From (1), we can conclude that the voltage across the resonant tank in the time domain is given by the sum of voltages across the capacitors C_r

$$\sum_k v_{C_r,k} = \sum_k \int_0^t \frac{i_{L_r,k}(\tau)}{C_r} d\tau = 0 \tag{2a}$$

and the sum of voltages across the inductors L_r

$$\sum_k v_{L_r,k} = \sum_k L_r \frac{di_{L_r,k}(t)}{dt} = 0. \tag{2b}$$

Taking the neutral point of the star as the reference point, we can calculate the voltage across the resonant tank and primary of each phase v_{kN}

$$\left.\begin{aligned} v_A - v_B &= v_{AN} - v_{BN} \\ v_B - v_C &= v_{BN} - v_{CN} \\ v_C - v_A &= v_{CN} - v_{AN} \\ v_{AN} + v_{BN} + v_{CN} &= 0 \end{aligned}\right\} v_{kN} = \frac{2v_k - \sum_{j \neq k} v_j}{3}. \tag{3}$$

Rectified voltages are trivial to calculate as the voltage at the output is forced by the rectifier, obtaining the phase voltages at the primaries as the voltage seen by their corresponding secondaries multiplied by the winding turn ratio (see Fig. 2).

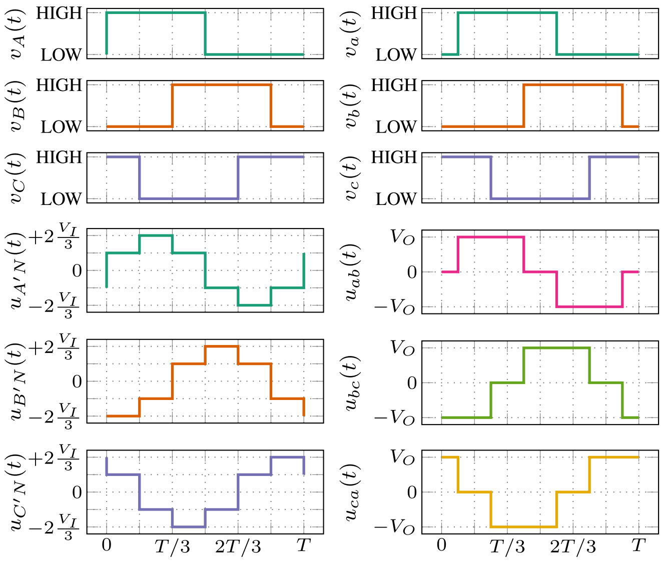

(a) (b)

Fig. 2. Voltages seen by the inverter and the rectifier (at resonance). (a) Inverter switching to neutral. (b) Rectifier into the secondary.

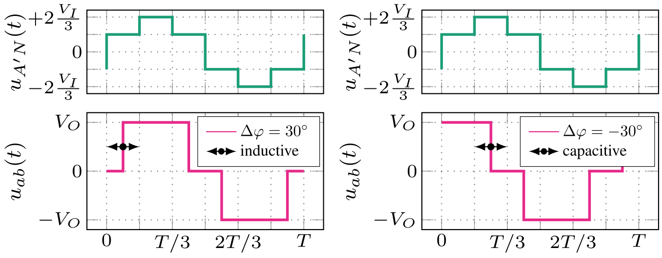

(a) (b)

Fig. 3. Voltages at both sides of the resonant tank referred to the neutral of the primary for different load types (inductive and capacitive). (a) Inductive behavior. (b) Capacitive behavior.

In Fig. 2, it is assumed that the converter operates at resonance and, consequently, the fundamental harmonic of the voltages from each switching node to the neutral on the primary and the voltage reflected from the secondary are in phase.

When this is happening, a phase delay of $\Delta\varphi = 30\,°$ between the gate signals at the primary and the secondary side is present. This delay in the gate pulses (between v_k and v_K in Fig. 3) is due to the nature of the wye–delta transformer ($30\,°$ phase-shift transformer).

When the converter is operating out of resonance, an additional phase delay between the inverter and the rectifier has to be performed to mimic the behavior of an ideal diode. Fig. 3 shows the two most relevant cases for inductive and capacitive behavior. In principle, six regions can be differentiated (three inductive $\Delta\varphi \in (0\,°, 180\,°]$ and three capacitive $\Delta\varphi \in (-180\,°, 0\,°]$), but in normal operation, only the first two inductive regions ($\Delta\varphi \in (0\,°, 120\,°]$) are relevant as the third only applies at low power and high frequency (non-narrow-frequency-range operation), while the capacitive defines the frontier between ZVS and zero-current switching (ZCS) operation.

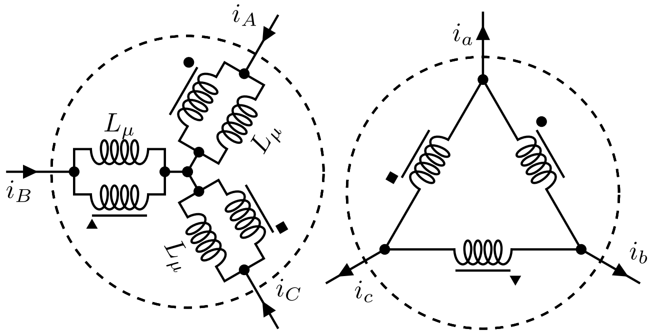

(a) (b)

Fig. 4. Three-phase transformer model with magnetizing inductance referred to the primary. (a) Primary in wye configuration. (b) Secondary in delta configuration.

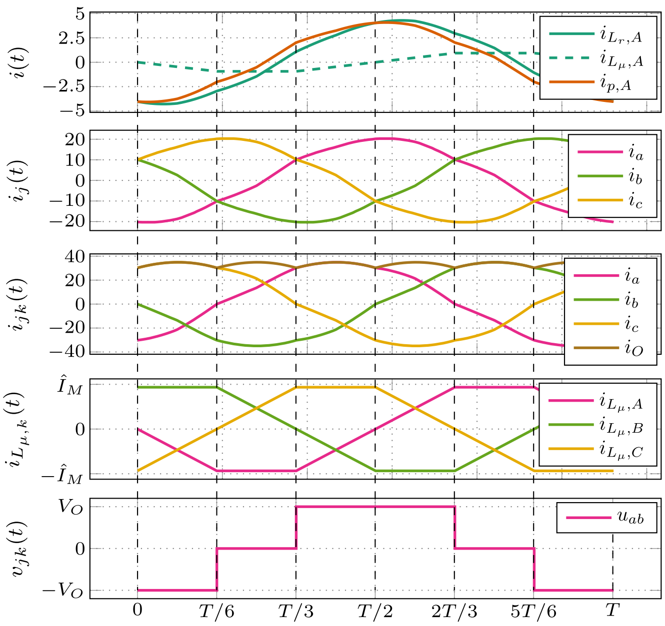

Fig. 5. Six-pulse three-phase rectifier behavior.

The transformer model used in further analysis is shown in Fig. 4, where a very low leakage inductance is considered (unity coupling factor between primaries and secondaries).

The voltage across the secondaries $u_{ab}(t)$, $u_{bc}(t)$, and $u_{ca}(t)$ induces a magnetic flux $v_{ij} = d\Phi_{ij}/dt$ on each phase of the transformer. According to the volt-second product of the core shown in u_{ab} (see Fig. 5), the peak of the B-field is given by

$$\Phi_{ij} = \int v_{ij}(t)dt \rightarrow V_O = \frac{\hat{B} n_s A_e}{T_S/6} \longrightarrow \hat{B} = \frac{V_O}{6 f_S n_s A_e}. \tag{4}$$

The same procedure can be repeated for the single phase LLC, this time, with half the period of volt-second product

$$\Phi_{ij} = \int v_{ij}(t)dt \rightarrow V_O = \frac{\hat{B} n_s A_e}{T_S/4} \longrightarrow \hat{B} = \frac{V_O}{4 f_S n_s A_e} \tag{5}$$

meaning that the B-field on the three-phase transformer core is 33% lower by evaluating the relationship between (4) and (5) than the single-phase LLC for the same transformer effective area A_e, output voltage V_O, and switching frequency f_S, providing us means to decrease the volume of the transformer.

Usually, the output capacitance C_L is big enough so that maximum output can be considered constant in steady state. Once the switching frequency f_S and the output voltage V_O are set, and the gain is required given that the input voltage V_I is within the possible range of gains, the inverter–rectifier delay $\Delta\varphi$ has a unique inductive solution ($\Delta\varphi > 0\,°$), and thus, the steady-state solution can be found according to the solution of the differential equation of the resonant tank [21]

$$i_{L_r,A}(t) = \frac{c_1}{Z_r}\sin(\omega_r t) + c_2\cos(\omega_r t) \tag{6a}$$

$$v_{C_r,A}(t) = v_{C_r,A}(0) + c_1\left[1 - \cos(\omega_r t)\right] + Z_r c_2 \sin(\omega_r t) \tag{6b}$$

$$v_{L_\mu,A}(t) = v_{L_\mu,A}(0) + n\int_0^t \frac{u_{ab}(t)}{L_\mu}dt \tag{6c}$$

where constants c_1 and c_2 are the initial voltage across the inductor and the initial current through the inductor, respectively

$$c_1 = V_I - v_{C_r,A}(0) - n u_{ab}(0) \tag{7a}$$

$$c_2 = i_{L_r,A}(0). \tag{7b}$$

The exact solution is obtained by ensuring the output current $i_O(t)$ continuous (C^0). This means that the switching patterns at the secondary match the behavior of an ideal diode. The topology is driven by the switching frequency of bridges and the delay between them to compensate for the input voltage and accomplish soft switching in the secondary. This is performed by imposing $+V_O$ across the winding i_j when $i_i > i_{k\neq i}$ and $-VO$ when $i_i < i_{k\neq i}$ as shown in Fig. 5, emulating the behaviour of an ideal three-phase diode rectifier.

The average output current is given by the integral of the six-pulse rectification

$$\frac{\hat{I}_O}{I_O} = \frac{1}{T/6}\int_{-\frac{T}{12}}^{\frac{T}{12}} \cos\left(2\pi\frac{t}{T}\right)dt = \frac{3}{\pi}. \tag{8}$$

The input current from the dc power supply is also a six-pulse current waveform. This means that the current stress of the input filter is dramatically improved from the single-phase LLC as only the harmonics multiple of six have to be filtered out.

B. Resonant Tank Gain

The topology behaves as a dc transformer (load independent) at resonance; this means that the reactive power is solely given by the magnetizing inductance of the transformer.

The operation out of resonance is required to fix the gain of the resonant tank and compensate the variation on the input voltage. This affects the reactive power in a way that frequencies above resonance will inductively load the input and capacitively under resonance.

Fig. 6 shows the exact resonant tank characteristic gain against the switching frequency according to (6).

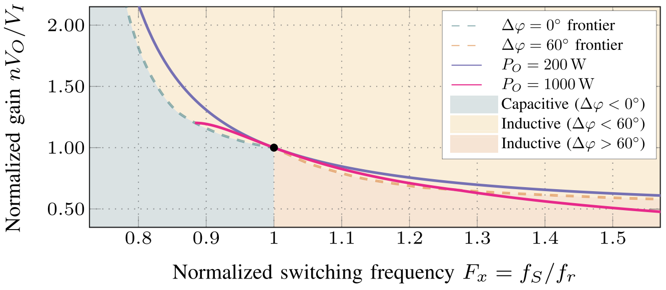

Fig. 6. Resonant tank characteristic gain as a function of the normalized switching frequency F_x.

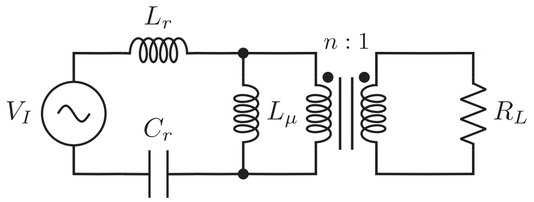

Fig. 7. Single-phase equivalent circuit (FHA) for a three-phase LLC converter in wye–delta.

C. Fundamental Harmonic Approximation

The analysis of LLC converters is typically started with fundamental harmonic approximation (FHA) as it provides a straightforward method to describe the converter gain as a function of switching frequency [22].

This process is well documented in the literature for the single-phase LLC, but it is usually summarized as follows:

$$\frac{nV_O}{V_I} = \frac{(m-1)\cdot F_x^2}{\sqrt{\left(mF_x^2 - 1\right)^2 + Q^2(m-1)^2F_x^2\cdot\left(F_x^2-1\right)^2}} \tag{9}$$

where the L_r, C_r, and L_μ design space is transformed into Z_r, m, and Q, with $m = 1 + L_\mu/L_r$ being the total-inductance-to-resonant-inductance ratio, F_x the normalized switching frequency, $Q = Z_r/R_{\text{eq}}$ the quality factor, and $R_{\text{eq}} = 8n^2/\pi^2 R_L$ the equivalent ac resistance reflected to the primary. Fig. 7 shows the equivalent FHA circuit for the three-phase LLC converter in wye–delta. As the power transmitted is split between the three phases, a single-phase FHA equivalent circuit is proposed.

The complete process though is obtained from impedance representation at the operating frequency f_S (fundamental harmonic) for which

$$\left.\begin{aligned} \bar{z}_r &= j\omega_o L_r + \frac{1}{j\omega_o C_r} \\ \bar{z}_o &= j\omega_o L_\mu || R_{\text{eq}} \end{aligned}\right\} \bar{U}_o = \frac{\bar{z}_o}{\bar{z}_o + \bar{z}_r}\cdot\bar{U}_i \tag{10}$$

where the real time-domain spectrum of $\bar{U}_i$ and $\bar{U}_o$ is known (given by a Fourier expansion)

$$\bar{U}_i = a_0 + jb_0. \tag{11}$$

For synchronous rectification, both voltages are square waveforms meaning that the magnitude of $\bar{U}_o$ must be multiplied by $\pi/(4n)$ to obtain V_O.

The same process can be repeated calculating the amplitude of the first harmonic of $v_{k'N}(t)$ as the input voltage

$$R_{eq,\mathrm{Y}\Delta} = 9\left(\frac{3}{\pi}\right)^2 \cdot n^2 R_L \tag{12a}$$

$$\frac{V_O}{|\bar{U}_o|} = \frac{2}{\pi}\sqrt{3}. \tag{12b}$$

D. Output Capacitance Selection

An initial approximation (for low ripple) on the voltage ripple is obtained by the integration of the difference of the input current from the rectifier and the output current to the load when the former is higher than its average value, defining $a = \hat{I}_O/I_O$

$$\begin{aligned}\Delta v_O(a) &= \frac{I_O}{\omega C_O}\int_{\sin^{-1}(a)}^{\pi-\sin^{-1}(a)} \sin\left(\omega_{\min} t\right) d(\omega t)\\ &= \frac{I_O}{\omega C_O}\left[2a\tan^{-1}\left(\frac{a}{\sqrt{1-a^2}}\right) + 2\sqrt{1-a^2} - a\cdot\pi\right]\end{aligned} \tag{13}$$

where a is calculated averaging the input current to the capacitor as in (8) for six-pulse rectification, where for the single-phase LLC, $a = 2/\pi$, while for the three-phase LLC, $a = 3/\pi$. Evaluating on (13), we get that for the same output voltage ripple, the three-phase LLC requires less than a 38.5% of what the single-phase LLC requires.

For the worst case full power output (1 kW) as specified in Table II, minimum switching frequency (810 kHz), and 1% voltage ripple (100 mV), a capacitance of 2 µF is needed. We selected 21 multi-layer ceramic capacitor (MLCC) 100-nF capacitors in parallel to achieve this capacitance (*CGA5L2C0G1H104J160AE*).

E. Design Rules of the Components

Every parameter of the converter has a big impact on the design. To unveil this entanglement, a design guideline is explained in this subsection with the purpose of clarifying the procedure. The main contribution of each parameter is listed as follows.

1) Transformer winding turn ratio n defines the voltage gain at resonance; due to the wide input voltage gain required, it is desirable that it operates in both step-down (above resonance) and step-up (below resonance).
2) Resonant inductance L_r contributes to the quality factor of the tank $Q = \omega L_r/R_{\text{eq}}$ and thus its selectivity.
3) Resonant capacitance C_r defines the resonant frequency of the tank and must be able to withstand the voltage across it due to the resonant current.
4) Magnetizing inductance L_μ defines the sensitivity of the gain, including the maximum boost of the LLC.

To calculate the current and voltage rating of the resonant tank, it can be assumed that the resonant current is dominant over the magnetizing current; through (8), its peak is given by

$$\hat{I}_{L_r} = \frac{\pi}{3\sqrt{3}}\frac{1}{n}\frac{P_O}{V_O} \tag{14a}$$

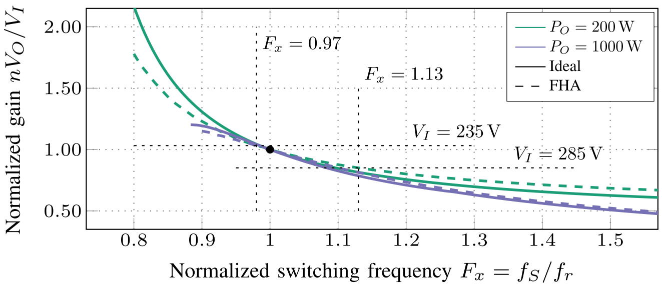

Fig. 8. Ideal and FHA characteristic gain of the converter.

TABLE III
DESIGN MADE TO COMPLY WITH THE SPECIFICATIONS

Parameter	Value	Description
L_r	9.6 µH	Inductance of the resonant tank
C_r	3.32 nF	Capacitance of the resonant tank
L_μ	12.0 µH	Magnetizing inductance
C_L	2 µF	Output capacitance
n_1	5	Number of turns of the primary
n_2	1	Number of turns of the secondary
Q_i	GS66508T	Inverter transistor
Q_r	BSZ018N04LS6	Rectifier transistor

and the voltage across the resonant capacitor is

$$\hat{V}_{C_r} = \frac{\hat{I}_{L_r}}{2\pi f_{\min} C_r}. \tag{14b}$$

The first step is to choose the winding turn ratio n, which, when selecting a single-turn secondary due to the high amplitude current on the secondary side, $n = 5$, is the only integer that centers the resonance within the gain range calculated from the input voltage range in normal operation.

For a first iteration of the converter and as a proof of concept, the maximum voltage across the capacitor was selected to 230 V, meaning that for a resonant frequency $f_r = 900$ kHz, the value for the resonant capacitor is $C_r = 3.32$ nF, and thus, $L_r = 9.6$µH.

With both $Z_r = \sqrt{L_r/C_r}$ and f_r decided, there only exists a single value of m that is capable of meeting the requirement of $\Delta F_x = 10\,\%$ for the input voltage and output power ranges. In this case, $m = 2.27$ making $L_\mu = 12$ µH.

The parameters of the topology were designed considering the maximum and minimum gains, as once ΔF_x is set for an input voltage and output power range, only one set of values for L_r, C_r, and L_μ is obtained. These gains are derived from Table II with (9) obtaining the response in Fig. 8. The designed values are listed in Table III.

III. MAGNETIC DESIGN

Unlike the resonant capacitor whose voltage and current ratings as well as capacitance are known and can be found in a parametric search, the design and optimization of L_r and L_μ requires a lot of calculation and simulation effort, even though the nominal lumped-model values are known.

Within the behavior of three-phase magnetics, and more predominantly, in planar magnetics, the potential for phase unbalance increases. This phenomenon significantly impacts the performance of power converters, requiring the development of compensation techniques to mitigate their effects.

This phenomenon manifests as voltage and current dependence between phases. When the synchronous rectifier forces the voltage across the secondary windings, if unbalanced, it results in an uneven storage of magnetizing energy among the phases. Consequently, unbalance becomes apparent during operation; nonetheless, the issue worsens in a three-phase inductor for the same unbalance, rather than the transformer itself. This is due to additional series coupling between two phases. For instance, the current flowing through phase k will induce an additional series voltage in the other phases, which are 120° apart from phase k, unbalancing the system.

This is because of the nonsymmetry of the typical three-phase magnetic core (three equal columns in an EE core), where one of the columns (central) presents a shorter magnetic path length to the three columns merging point compared with the other columns (laterals). To overcome this, in this section, a comprehensive analysis is made to address nonsymmetrical magnetic core structures and achieve optimal performance.

A. Gapped Three-Port Asymmetric Magnetic Core

Three-phase core architectures require to have three independent magnetic paths, and this is translated into an architecture with three winding positions usually referred to as three ports.

In general, it is desirable that balanced three-phase magnetic components are built upon symmetric structures, such as delta or wye cores [23]. Nonetheless, these constructions have higher volume and inconvenient terminations for windings in a linear downstream circuit topology.

The utilization of nonsymmetrical magnetic core structures leads to noncompensated magnetic component; this fact is relevant as it is detrimental to the balancing of phases.

In the case of the synchronous three-phase LLC converter, each phase has its current shifted, unbalancing the soft switching of the inverter (different switching currents on the three-phase bridge leading to loss of ZVS) and the currents in the secondary (risk of losing its quasi-ZCS). Altogether, a symmetric magnetic component in a three-phase system contributes to the minimization of unbalance between phases, ultimately reducing the power losses and thus, improving its thermal stability.

In [18], a three-column EE core was built with two different soft materials in order to compensate magnetic coupling between columns. The same effect can be accomplished by narrowing the central column with respect to laterals as the equivalent reluctance seen from the null flux singular point of the core is compensated.

In this subsection, geometry compensation is derived for two three-port core geometries: the EE core and the EI core. An alternative approach is developed in the Appendix. Core dimensioning is shown in Fig. 9.

The mathematical analysis is performed based on the magnetostatic problem for which Ampère's law (15) and the magnetic flux conservation law (16) are used

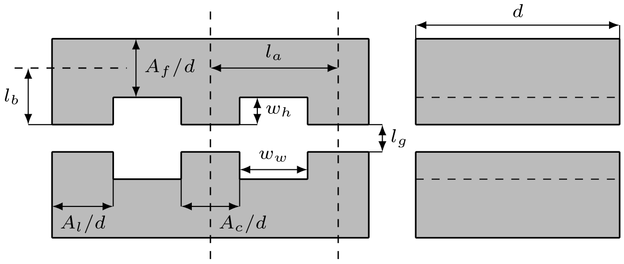

(a) (b)

Fig. 9. EE core dimensioning. (a) Front view. (b) Side view.

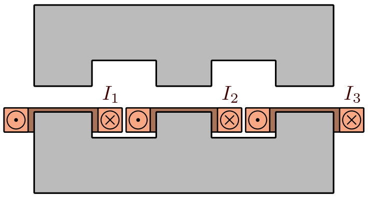

Fig. 10. Winding layout.

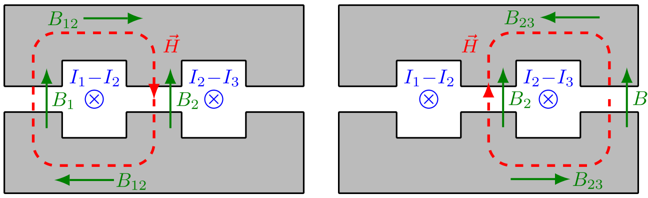

(a) (b)

Fig. 11. Definition of the signs of the H-field and the current through the window. (a) Left current loop. (b) Right current loop.

$$\oint_L H dl = \oiint_S J \, dS \tag{15}$$

$$\oiint_S B \, dS = 0. \tag{16}$$

All the analysis are made considering the fringing with σ_l and σ_c correction factors, reserved for future analysis in this subsection.

To simplify the analysis and make it more comprehensible, an approach regarding the winding layout in this section was adopted. Instead of detailing the winding layout for each individual phase, the winding arrangement was considered as one phase for each column. Fig. 10 provides a visual representation of this simplified winding layout, illustrating how we treated the windings as a single phase within each column, highlighting the connections and relationships that are relevant to our analysis and design.

Evaluating the H-loops defined in Fig. 11 with (15), we obtain the first two equations

$$\left(\frac{l_g}{\sigma_l} + \frac{2l_b}{\mu_r}\right)\frac{B_1}{\mu_0} + \frac{2l_a}{\mu_r}\frac{B_{12}}{\mu_0} - \left(\frac{l_g}{\sigma_c} + \frac{2l_b}{\mu_r}\right)\frac{B_2}{\mu_0} = I_1 - I_2 \tag{17}$$

$$\left(\frac{l_g}{\sigma_l}+\frac{2l_b}{\mu_r}\right)\frac{B_3}{\mu_0}+\frac{2l_a}{\mu_r}\frac{B_{23}}{\mu_0}-\left(\frac{l_g}{\sigma_c}+\frac{2l_b}{\mu_r}\right)\frac{B_2}{\mu_0}=I_2-I_3. \tag{18}$$

To complete the system, we apply (16) to the junction magnetic paths between columns

$$B_{12}=B_1\cdot\frac{A_l}{A_f} \tag{19a}$$

$$B_{23}=B_3\cdot\frac{A_l}{A_f} \tag{19b}$$

and to the singular spot where the three magnetic fluxes of the columns meet

$$B_1\cdot A_l+B_2\cdot A_c+B_3\cdot A_l=0. \tag{19c}$$

Equation (19) can be substituted into (17) and (18) and together with (19c); a system of three linear equations with B_1, B_2, and B_3 (B-field for each column) is defined as

$$\mathbf{A}\mathbf{x}=\mathbf{b}\longrightarrow\mathbf{x}=\mathbf{A}^{-1}\cdot\mathbf{b} \tag{20a}$$

$$\begin{cases} a_{11}=\frac{1}{\mu_0}\left[\frac{l_g}{\sigma_l}+\frac{2l_b}{\mu_r}+\frac{2l_a}{\mu_r}\frac{A_l}{A_f}\right]\\ a_{23}=a_{11}\\ a_{12}=\frac{l_g}{\sigma_c}+\frac{2l_b}{\mu_r}\\ a_{22}=a_{12}\end{cases} \tag{20b}$$

$$\mathbf{A}=\begin{bmatrix}a_{11}&a_{12}&0\\0&a_{22}&a_{23}\\A_l&A_c&A_l\end{bmatrix},\ \mathbf{x}=\begin{bmatrix}B_1\\B_2\\B_3\end{bmatrix},\ \mathbf{b}=\begin{bmatrix}I_1-I_2\\I_2-I_3\\0\end{bmatrix}. \tag{20c}$$

The B-field now is completely defined and solved with (20a). To fill the inductance matrix $\mathbf{L}$ of (21) for a three-column single-turn magnetic component, we define the flux on each column j (ϕ_{ij}) and divide it by the current I_i that causes it obtaining (22)

$$\mathbf{L}_t=\begin{bmatrix}L_{ll}&M_{lc}&M_{ll}\\M_{lc}&L_{cc}&M_{lc}\\M_{ll}&M_{lc}&L_{ll}\end{bmatrix} \tag{21}$$

$$L_{ll}=\left.\frac{\phi_1}{I_1}\right|_{\substack{I_2=0\\I_3=0}}\approx+\mu_0\frac{A_l(A_c+A_l)}{l_g(2A_l+A_c)} \tag{22a}$$

$$L_{cc}=\left.\frac{\phi_2}{I_2}\right|_{\substack{I_1=0\\I_3=0}}\approx+\mu_0\frac{2A_cA_l}{l_g(2A_l+A_c)} \tag{22b}$$

$$M_{ll}=\left.\frac{\phi_1}{I_3}\right|_{\substack{I_2=0\\I_3=0}}\approx-\mu_0\frac{A_l^2}{l_g(2A_l+A_c)} \tag{22c}$$

$$M_{lc}=\left.\frac{\phi_1}{I_2}\right|_{\substack{I_1=0\\I_3=0}}\approx-\mu_0\frac{A_cA_l}{l_g(2A_l+A_c)}. \tag{22d}$$

This approximation represents the effect of an ideal magnetic core ($\mu_r\rightarrow+\infty$). The complete solution to (20a) can be solved to get $M_{lc}=M_{ll}$, for which the lateral column must shrink in the quantity

$$A_l^*=A_c\cdot\frac{A_f\left(2\frac{l_b}{\mu_c}+\frac{l_g}{\sigma_l}\right)}{A_f\left(2\frac{l_b}{\mu_c}+\frac{l_g}{\sigma_c}\right)-2A_c\frac{l_a}{\mu_c}} \tag{23}$$

where a minimum air-gap length is required to be extracted from nulling of the denominator of (23)

$$l_g\geq\sigma_c\cdot\frac{2}{\mu_r}\left(\frac{A_c}{A_f}l_a-l_b\right). \tag{24}$$

When (23) is satisfied, we can calculate the exact solution for (22) as follows:

$$L_{ll}=\left.\frac{\phi_1}{I_1}\right|_{\substack{I_2=0\\I_3=0\\A_l=A_l^*}}=+\mu_0\frac{2}{3}\frac{A_c}{\frac{l_g}{\sigma_c}+\frac{2l_b}{\mu_c}} \tag{25a}$$

$$L_{cc}=\left.\frac{\phi_2}{I_2}\right|_{\substack{I_1=0\\I_3=0\\A_l=A_l^*}}=+\mu_0\frac{2}{3}\frac{A_c}{\frac{l_g}{\sigma_c}+\frac{2l_b}{\mu_c}} \tag{25b}$$

$$M_{ll}=\left.\frac{\phi_1}{I_3}\right|_{\substack{I_2=0\\I_3=0\\A_l=A_l^*}}=-\mu_0\frac{1}{3}\frac{A_c}{\frac{l_g}{\sigma_c}+\frac{2l_b}{\mu_c}} \tag{25c}$$

$$M_{lc}=\left.\frac{\phi_1}{I_2}\right|_{\substack{I_1=0\\I_3=0\\A_l=A_l^*}}=-\mu_0\frac{1}{3}\frac{A_c}{\frac{l_g}{\sigma_c}+\frac{2l_b}{\mu_c}}. \tag{25d}$$

An accurate representation of the air-gap effect in the coupling of windings is essential when designing the components. For such a task, two correction factors were introduced previously into the analysis made in the present article denoted by σ_l and σ_c for the lateral and central columns, respectively.

In [24], a simplified method for calculating the reluctance of the air gap was described based on the Schwarz–Christoffel transformation for infinitely long magnetic cores (2-D). A similar approach was taken in [25] where the aforementioned work is extrapolated into both directions of the cross section of the air gap. Applying it into our problem, we get the correction factor of the effective air gap in the central column

$$\sigma_{xc}=\frac{a_c\cdot\pi}{a_c\cdot\pi+2l_g\cdot\left(1+\ln\left(\pi\frac{2l_b-a_f}{4l_g}\right)\right)} \tag{26a}$$

$$\sigma_{yc}=\frac{d\cdot\pi}{d\cdot\pi+2l_g\cdot\left(1+\ln\left(\pi\frac{2l_b+a_f}{4l_g}\right)\right)} \tag{26b}$$

$$\sigma_c=\sigma_{xc}\cdot\sigma_{yc} \tag{26c}$$

and in the lateral columns

$$\sigma_{xl}=\frac{a_l\cdot\pi}{a_l\cdot\pi+2l_g\cdot\left(1+\ln\left(\pi\frac{2l_b-a_f}{4l_g}\right)\right)} \tag{27a}$$

$$\sigma_{yl}=\frac{d\cdot\pi}{d\cdot\pi+2l_g\cdot\left(1+\ln\left(\pi\frac{2l_b+a_f}{4l_g}\right)\right)} \tag{27b}$$

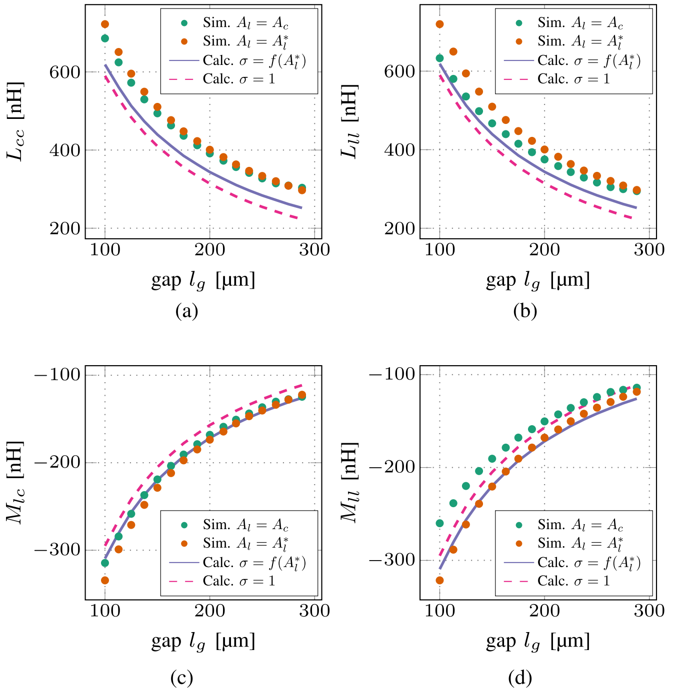

Fig. 12. Comparison of inductance matrix components calculated with (23) and the obtained in a magnetostatic ANSYS simulation sweeping $A_l^* = f(l_g)$ and $A_l = A_c$. (a) Central self-inductance L_{cc}. (b) Lateral self-inductance L_{ll}. (c) Lateral–central M_{lc}. (d) Lateral–lateral M_{ll}.

$$\sigma_l = \sigma_{xl} \cdot \sigma_{yl}. \tag{27c}$$

Fig. 12 shows the comparison between the mutual inductances M_{lc} and M_{ll}. The application of this expression leads to a 5% maximum error without compensating for the fringing effect.

Once the methodology to compensate the asymmetry of a planar EE core is established and including the effect of the fringing in the coupling, geometry dimensioning (25) is validated via finite-element simulation. The simulations were performed in Maxwell 3D with minimal track width to discard the effect of the inductance added by the windings.

The results are represented in Fig. 12; the mutual inductances M_{ll} and M_{lc} show that M_{lc} does not significantly depend on the size of the lateral column A_l, while M_{ll} varies up to a 15%, reducing the maximum error to a 7.5%. These cases can be observed when comparing $\sigma = f(A_l^*)$ (fringing effect considered) with the simulated results $A_l = A_l^*$, demonstrating the predictability of the proposed model. With it, the transformer and resonant inductor designs can proceed.

1) Wye–Delta Transformer: A single-phase transformer can be represented as the quadrupole given by (28) with $\mathbf{u} = \mathbf{Z}_{1\phi} \cdot \mathbf{i}$

$$\mathbf{Z}_{1\phi} = \begin{bmatrix} \bar{z}_{pp} & \bar{z}_{ps} \\ \bar{z}_{sp} & \bar{z}_{ss} \end{bmatrix}. \tag{28}$$

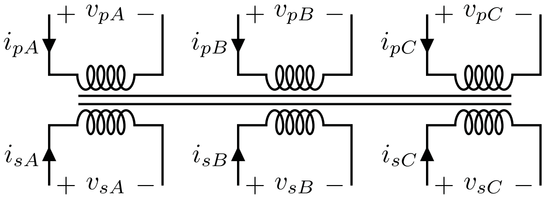

Fig. 13. Six arbitrarily coupled inductors.

In general, a three-phase transformer is electrically analyzed by assuming it to be balanced (equivalent to a single phase). No matter how the windings are coupled (see Fig. 13), we can define a 6×6 matrix for the six windings (three primaries and three secondaries)

$$\mathbf{Z}_{6\mu} = \begin{bmatrix} \mathbf{Z}_{AA} & \mathbf{Z}_{AB} & \mathbf{Z}_{AC} \\ \mathbf{Z}_{BA} & \mathbf{Z}_{BB} & \mathbf{Z}_{BC} \\ \mathbf{Z}_{CA} & \mathbf{Z}_{CB} & \mathbf{Z}_{CC} \end{bmatrix}, \ \mathbf{Z}_{jk} = \begin{bmatrix} \bar{z}_{p_j p_k} & \bar{z}_{p_j s_k} \\ \bar{z}_{s_j p_k} & \bar{z}_{s_j s_k} \end{bmatrix} \tag{29a}$$

$$\begin{aligned} \mathbf{u} &= \begin{bmatrix} \mathbf{u}_A & \mathbf{u}_B & \mathbf{u}_B \end{bmatrix}^T \\ &= \begin{bmatrix} \bar{U}_A & \bar{U}_a & \bar{U}_B & \bar{U}_b & \bar{U}_C & \bar{U}_c \end{bmatrix}^T \end{aligned} \tag{29b}$$

$$\begin{aligned} \mathbf{i} &= \begin{bmatrix} \mathbf{i}_A & \mathbf{i}_B & \mathbf{i}_C \end{bmatrix}^T \\ &= \begin{bmatrix} \bar{I}_A & \bar{I}_a & \bar{I}_B & \bar{I}_b & \bar{I}_C & \bar{I}_c \end{bmatrix}^T \end{aligned} \tag{29c}$$

$$\mathbf{u} = \mathbf{Z}_{6\mu} \cdot \mathbf{i} \tag{29d}$$

equivalent to a block matrix produced by the merge of the three pairs of primaries and secondaries. In order for $\mathbf{Z}_{6\mu}$ to behave as three independent single-phase transformers, an equivalent matrix has to be found so that only the main diagonal is filled while null matrices $\mathbf{O}_{2\times2}$ fill the rest

$$\mathbf{Z}_{3\phi} = \begin{bmatrix} \mathbf{Z}^*_{AA} & \mathbf{O}_{2\times2} & \mathbf{O}_{2\times2} \\ \mathbf{O}_{2\times2} & \mathbf{Z}^*_{BB} & \mathbf{O}_{2\times2} \\ \mathbf{O}_{2\times2} & \mathbf{O}_{2\times2} & \mathbf{Z}^*_{CC} \end{bmatrix}. \tag{30}$$

If it is assumed that the primary and secondary windings are perfectly coupled (no leakage), then the equivalent circuit can be represented, as shown in Fig. 4.

The condition that we need is that the sum of currents for the three primaries or three secondaries null each other (Kirchhoff's current law), i.e.,

$$\mathbf{i}_A + \mathbf{i}_B + \mathbf{i}_C = \begin{bmatrix} 0 \\ 0 \end{bmatrix} \begin{cases} \bar{I}_A + \bar{I}_B + \bar{I}_C = 0 \\ \bar{I}_{A'} + \bar{I}_{B'} + \bar{I}_{C'} = 0. \end{cases} \tag{31}$$

If we assume that (30) will be satisfied within the definition of (29d), then we can split the block matrix $\mathbf{Z}_{6\mu}$ as follows:

$$\mathbf{Z}_{6\mu} = \begin{bmatrix} \mathbf{Z}_{AA} & \mathbf{O}_{2\times2} & \mathbf{O}_{2\times2} \\ \mathbf{O}_{2\times2} & \mathbf{Z}_{BB} & \mathbf{O}_{2\times2} \\ \mathbf{O}_{2\times2} & \mathbf{O}_{2\times2} & \mathbf{Z}_{CC} \end{bmatrix} + \begin{bmatrix} \mathbf{O}_{2\times2} & \mathbf{Z}_{AB} & \mathbf{Z}_{AC} \\ \mathbf{Z}_{BA} & \mathbf{O}_{2\times2} & \mathbf{Z}_{BC} \\ \mathbf{Z}_{CA} & \mathbf{Z}_{CB} & \mathbf{O}_{2\times2} \end{bmatrix}. \tag{32}$$

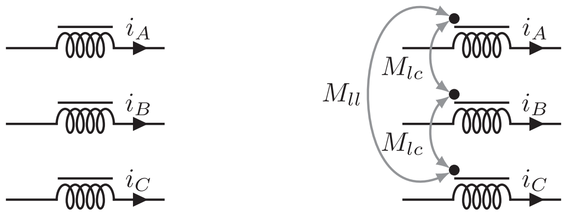

(a) (b)

Fig. 14. Three-phase coupled inductor electrical model. (a) Three single phase. (b) Single three phase.

It is trivial that $\mathbf{Z}_{ij} = \mathbf{Z}_{ji}$ and can be demonstrated that, due to the axial symmetry of an EE or EI core, $\mathbf{Z}_{AB} = \mathbf{Z}_{CB}$ as the mutual inductance between the central column B, and each of the two lateral columns (A and C) is the same. This leads us to the reduction of the last equation to a lateral-to-lateral mutual block matrix $\mathbf{Z}_{ll}$ and to a lateral-to-central block matrix $\mathbf{Z}_{lc}$; we can define a block matrix $\Delta\mathbf{Z} = \mathbf{Z}_{ll} - \mathbf{Z}_{lc}$ so that previous equation is simplified to

$$\mathbf{Z}_{6\mu} = \begin{bmatrix} \mathbf{Z}_{AA} & \mathbf{O}_{2\times2} & \mathbf{O}_{2\times2} \\ \mathbf{O}_{2\times2} & \mathbf{Z}_{BB} & \mathbf{O}_{2\times2} \\ \mathbf{O}_{2\times2} & \mathbf{O}_{2\times2} & \mathbf{Z}_{CC} \end{bmatrix} + \underset{\mathbf{O}_{3\times3}}{\begin{bmatrix} \cancel{\mathbf{Z}_{lc}} & \mathbf{Z}_{lc} & \mathbf{Z}_{lc} \\ \mathbf{Z}_{lc} & \cancel{\mathbf{Z}_{lc}} & \mathbf{Z}_{lc} \\ \mathbf{Z}_{lc} & \mathbf{Z}_{lc} & \cancel{\mathbf{Z}_{lc}} \end{bmatrix}} + \begin{bmatrix} -\mathbf{Z}_{lc} & \mathbf{O}_{2\times2} & \Delta\mathbf{Z} \\ \mathbf{O}_{2\times2} & -\mathbf{Z}_{lc} & \mathbf{O}_{2\times2} \\ \Delta\mathbf{Z} & \mathbf{O}_{2\times2} & -\mathbf{Z}_{lc} \end{bmatrix}. \tag{33}$$

Due to (31), it is straightforward to demonstrate that the matrix full of $\mathbf{Z}_{lc}$ does not contribute in the voltage $\mathbf{u}$ when (29d) is applied. Also, if we want $\Delta\mathbf{Z} = \mathbf{O}_{2\times2}$, the only option is that the mutual inductance between lateral columns and that between a lateral and the central take the same value, which corresponds to a prior solution demonstrated in (23), which has been previously obtained by the customization of the columns.

Once the single-turn self and mutual inductances are obtained, the multi-turn case is derived by multiplying the mutual amount of turns to complete the flux in the magnetic core $\psi = n^1 \cdot n^2\phi$, obtaining an equivalent impedance matrix to the single-phase case in (28),

$$\mathbf{Z}^*_{kk} = j\omega \begin{bmatrix} n_p^2 & n_p n_s \\ n_p n_s & n_s^2 \end{bmatrix} \cdot (L_{ll} - M_{lc}) \tag{34a}$$

$$L^*_\mu = n_p n_s \cdot (L_{ll} - M_{lc}) = \mu_0 \frac{n_p n_s}{\dfrac{l_g}{\sigma_c A_c} + \dfrac{2 l_b}{\mu_c A_c}}. \tag{34b}$$

2) Three-Phase Inductor: As previously mentioned, the use of three single-phase resonant inductors, although straightforward, does not take advantage of the features of a three-phase system. A three-phase inductor is designed to merge the three single-phase inductors, as shown in Fig. 14. In this section, a brief analysis mimicking the one for the transformer is performed.

The real behavior of a three-phase inductor is given in Fig. 14(b) in order to be equivalent to three single-phase inductors, as in Fig. 14(a)

$$\mathbf{Z}_{3\phi} = \begin{bmatrix} \bar{z}^*_{AA} & 0 & 0 \\ 0 & \bar{z}^*_{BB} & 0 \\ 0 & 0 & \bar{z}^*_{CC} \end{bmatrix} \tag{35}$$

equivalent to (30) and

$$\mathbf{Z}_{3\mu} = \begin{bmatrix} \bar{z}_{AA} & \bar{z}_{AB} & \bar{z}_{AC} \\ \bar{z}_{BA} & \bar{z}_{BB} & \bar{z}_{BC} \\ \bar{z}_{CA} & \bar{z}_{CB} & \bar{z}_{CC} \end{bmatrix}. \tag{36}$$

Equation (31) is still valid as the primary of the transformer is connected to the inductor, so defining $\Delta\bar{z} = \bar{z}_{ll} - \bar{z}_{lc}$, we can split the above equation as follows:

$$\mathbf{Z}_{3\mu} = \begin{bmatrix} \bar{z}_{AA} & 0 & 0 \\ 0 & \bar{z}_{BB} & 0 \\ 0 & 0 & \bar{z}_{CC} \end{bmatrix} + \underset{\mathbf{O}_{3\times3}}{\begin{bmatrix} \cancel{\bar{z}_{lc}} & \bar{z}_{lc} & \bar{z}_{lc} \\ \bar{z}_{lc} & \cancel{\bar{z}_{lc}} & \bar{z}_{lc} \\ \bar{z}_{lc} & \bar{z}_{lc} & \cancel{\bar{z}_{lc}} \end{bmatrix}} + \begin{bmatrix} -\bar{z}_{lc} & 0 & \Delta\bar{z} \\ 0 & -\bar{z}_{lc} & 0 \\ \Delta\bar{z} & 0 & -\bar{z}_{lc} \end{bmatrix}. \tag{37}$$

Again, (23) makes $\Delta\bar{z} \equiv 0$ obtaining the equivalent self-inductance for column k

$$\bar{z}^*_{kk} = j\omega \cdot n_l^2 \left(L_{ll} - M_{lc}\right) \tag{38a}$$

$$L^*_r = n_l^2 \left(L_{ll} - M_{lc}\right) = \mu_0 \frac{n_l^2}{\dfrac{l_g}{\sigma_c A_c} + \dfrac{2 l_b}{\mu_c A_c}} \tag{38b}$$

where n_l is the number of turns of windings.

B. Core Losses

In general, core losses are facilitated as volumetric power losses given by the manufacturer's datasheet. Nonetheless, these data are usually condensed into the Steinmetz equation

$$P_V = k \cdot f^\alpha \cdot B^\beta \tag{39}$$

or into the improved generalized Steinmetz equation for nonsinusoidal operation

$$P_V = \frac{1}{T} \int_0^T k_i \left| \frac{dB}{dt} \right|^\alpha \cdot \Delta B^{\beta-\alpha} dt \tag{40a}$$

$$k_i = \frac{k}{(2\pi)^{\alpha-1} \displaystyle\int_0^{2\pi} |\cos(\theta)|^\alpha 2^{\beta-\alpha} d\theta}. \tag{40b}$$

In order to get more accurate representations of core losses, the data acquisition system used by the MagNet project from Princeton University [26] was used. The material was tested with an arbitrary signal generator to generate a trapezoidal B-field on the material ML91S (see Fig. 15). A curve fitting was performed obtaining $k = 0.320836$, $\alpha = 1.7106$, and $\beta = 3.24364$ for (39).

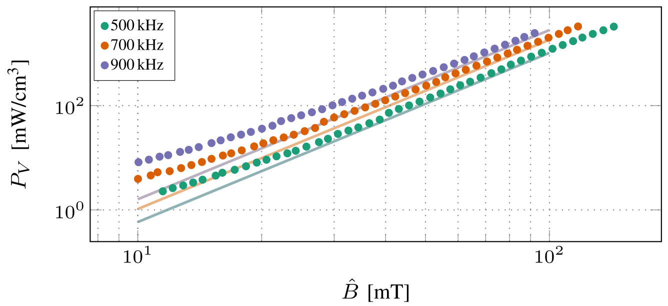

Fig. 15. Experimental power losses measured at 90 °C for a symmetric trapezoidal B-field waveform of $\hat{B}$ peak.

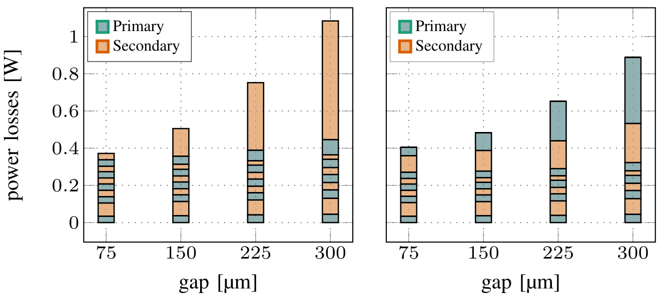

(a)

(b)

Fig. 16. Winding losses for the same EE core depending on the winding strategy (900 kHz). The bar stack represents the layers of the PCB. (a) PSPSPSPSPS. (b) PSPSPSPSP.

C. Core Geometry

Usually, multiple magnetic parts are used as building blocks to constitute the geometry of the core. In such cases, an unavoidable air gap is present; moreover, in order to design a balanced three-phase inductor or transformer, a minimum gap is mandatory as exposed in (24).

Although a distributed air gap [27] can reduce local fringing, it leads to higher complexity in the manufacturing of a custom core and reduces the robustness. By simply placing the conductors far away enough from the air gap, for example, by using an EI core instead of EE core, the fields intersecting the windings decay significantly leading to lower losses.

D. Winding Strategy

For planar magnetic cores in high-frequency applications, the solid wire solution becomes inconvenient as the current stress required in the windings increases in amplitude and harmonic content. The skin effect alone makes the maximum wire diameter to be AWG36 at 1 MHz (127 μm in diameter), requiring a high number of wires in parallel leading into higher proximity and worsening the termination effect [28].

Although Litz wire is a good solution due to its performance at high frequency, it compromises the economic viability of the converter. Printed circuit board (PCB) windings are less expensive, easily customizable, and ideal to create interleaving structures within the winding. For the converter presented, a 5:1 windings' turn ratio for the transformer has to be implemented, for which PCB windings are chosen.

In order to make interleaving, the secondary turn is split into five turns to obtain the same current and compensate the increase in the H-field of the primary turns. Nonetheless, due to the asymmetry of this arrangement, this makes it more susceptible to external fields. Instead, the secondary turn can be split into four turns, leaving two primary turns enveloping with the top and bottom layers and the rest of the winding turns in the PCB.

For high-frequency currents, the contribution of the skin and proximity in the power losses breakdown becomes very noticeable. This is especially important in regions of strong magnetic fields (proximity to the air gap). A set of simulations was run varying the air gap with a fringing effect close to the top layer of the PCB (see Fig. 16). This is made for two strategies (PSPSPSPSPS and PSPSPSPSP). The result depends heavily on the size of the gap and the distance from the winding to it.

Although an initial approximation can be obtained for foil conductors (PCB tracks) with analytical equations [29], fringing losses play a big role in the optimization of winding losses. Efforts in fringing power loss estimation are discussed in the literature for planar magnetics [30]. Nonetheless, the highest accuracy is returned by finite-element method simulations.

E. PCB Track Losses

Proximity and skin effects in high-current high-frequency designs have a big impact in the losses. For foil conductors (PCB tracks), a set of analytical equations for skin effect is derived in [29]

$$R_{\mathrm{DC}} = \frac{\rho_{\mathrm{Cu}}}{A_{\mathrm{eq}}} l_{\mathrm{eq}} \tag{41a}$$

$$\delta = \sqrt{\frac{\rho_{\mathrm{Cu}}}{\pi f \mu_{\mathrm{Cu}}}} \tag{41b}$$

$$P_{\mathrm{skin}} = R_{\mathrm{DC}} \cdot F_R \cdot \hat{I}^2 \tag{41c}$$

$$F_R = \frac{\nu}{4} \frac{\sinh(\nu) + \sin(\nu)}{\cosh(\nu) - \cos(\nu)}, \ \nu = \frac{t}{\delta} \tag{41d}$$

where F_R is a corrective factor, t is the thickness of the copper track (2 oz/ft), δ is the skin depth, ρ_{Cu} is the resistivity of copper, and μ_{Cu} is its absolute magnetic permeability of copper.

Due to the low voltage at the output compared to the input voltage, high frequency and high currents will be manifested in the rectifier circuit. Higher currents tend to focus on the sides of the track leading to higher RMS current and, thus, higher power losses.

Flux cancellation designs, such as in [31], are an option when parallelizing many transistors, and more PCB layers are available at the cost of producing higher complexity layouts. In the present work, a first prototype was designed with current orthogonality executed as much as possible to minimize the proximity losses.

The purely ohmic loss obtained in a simulation performed in ANSYS with 36 A peak and 900 kHz returned 4.53 W. Evaluating (41) for pieced sections of the conduction path (different

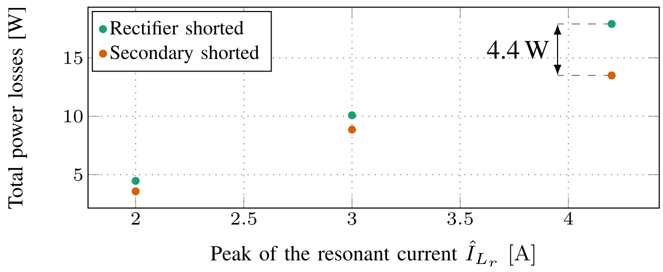

Fig. 17. Experimental PCB power losses as functions of a three-phase injected sinusoidal current at 900 kHz.

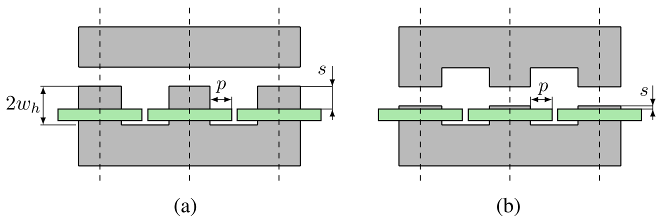

Fig. 18. Extra design space parameters of the design. (a) EI core. (b) EE core.

$l_{\rm eq}$ and $A_{\rm eq}$) returned 4.5 W. Testing this experimentally is also possible as three-phase currents can be achieved with the already built-in resonant tank:

1) short-circuiting the transistors in the inverter and allowing the current to rush-in into the tracks of the rectifier;
2) short-circuiting the three output terminals of the secondary windings.

In both cases, as in a three-phase system fault, the current will be strictly limited by the impedance of short circuit (the impedance of the rectifier board in the first case and the impedance of the windings in the second case). To avoid it, the current at the primary (resonant tank) was kept at a certain value peaking at 4.2 A, which will translate into 36 A in the secondary. This way, the primary is stressed in the same way and the power losses of the inverter, resonant tank, and transformer can be crossed-out of the equation discriminating the power losses of the rectifier board.

Fig. 17 shows the power losses with the two aforementioned experiments; for the primary current at full load, 4.4 W was obtained, defining a 0.5% of efficiency loss for 1-kW operation.

IV. PARETO-OPTIMAL DESIGN

An EE core was taken as reference to calculate the main design parameter of a three-phase planar transformer. Nonetheless, an EE core and an EI core are equivalent, so the same equation can be applied by making the equivalence.

A. Design Space

As it is a height-constrained core ($h = 12.9$ mm), we can show from Fig. 9 that the design has six degrees of freedom that have to be defined:

1) depth of the core d;
2) width of the window w_w;
3) half the height of the window w_h;
4) area of the central column $A_c = a_c \cdot d$;
5) area of the lateral column $A_l = a_l \cdot d$;
6) air-gap length l_g.

We can then discuss the mandatory constraints of the design, as follows.

1) *Central column shrinkage:* Equation (23) shows the relationship between the lateral and central columns as a function of l_g.
2) *Thermal dissipation capabilities:* This will define the maximum allowed B-field in the column through the power losses of the core. Estimating it can be tricky as accurate models (simulations) sheltered by experimental tests have to be performed, where 500 mW/cm^3 is a good starting point for planar magnetics with natural convection.
3) *Inductance:* The air gap is given by (38b) or (34b) depending on if it is an inductance or a transformer, respectively.

The parameters left are controlled defining the design space below and represented in Fig. 18 .

1) Air gap l_g is discretized to the gap spacer thickness.
2) *PCB track width p (window width):* Depending on the winding strategy, a minimum width in the window is required to fit the conductors.
3) *Air-gap proximity to the windings s (window height):* Shorter windows tend to have higher winding losses due to the proximity of the gap (fringing), but making it higher will be translated into a deeper core (longer windings scaling winding losses proportionally).

B. Optimization

Optimization was performed via a smart algorithm capable of calculating current excitations via a preliminary $\mathbf{Z}$ matrix obtained in ANSYS (refinement). This guarantees an accurate representation of voltage between winding terminals and, thus, core losses.

The design space was restricted according to the maximum dimensions of the machinery used in the manufacturing of custom cores (less than 30 mm) as well as the height-constrained design (less than 12.9 mm) to achieve a half-brick form factor.

Fig. 19 shows the power losses as well as the winding strategy. Being the PSPSPSPSP case more power-efficient in the window (air gap). At lower fringing fields, an additional parallel in the secondary reduces $R_{\rm DC}$ enough to compensate for these effects.

The same core geometries were simulated for both the transformer and the inductor; for the final design of the three-phase inductor and transformer, the same custom core was chosen whose dimensions can be found in Table IV and assembled by stacking cores (two in the case of the transformer and three in the case of the inductor with five turns).

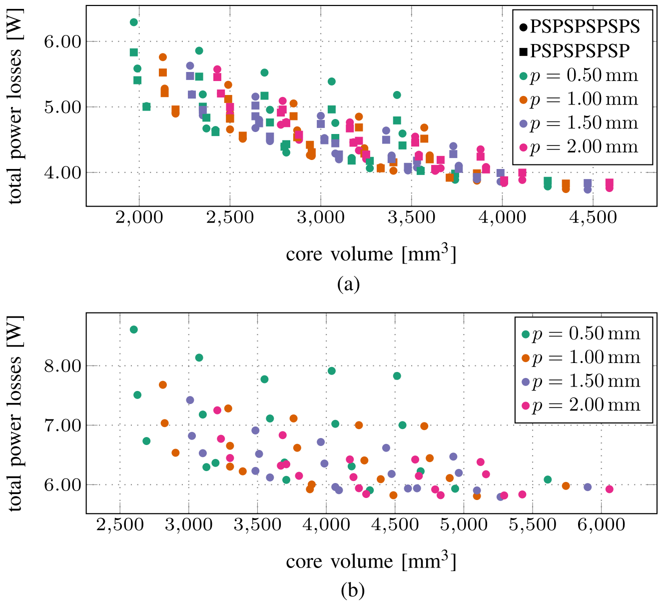

Fig. 19. Pareto front of the three-phase inductor and three-phase transformer with an EE core. (a) Transformer Pareto front. (b) Inductor Pareto front.

TABLE IV
OPTIMIZED THREE-COLUMN EI CORE DIMENSIONS

Parameter	Value	Description
w_w	7.1 mm	Window width
w_h	3.8 mm	Window height
A_f/d	4.5 mm	Junction column width
A_c/d	4.5 mm	Central column width
A_l/d	5.3 mm	Lateral column width
l_g	150 µm	Designed air-gap
d	8 mm	Depth of the core

V. IMPLEMENTATION

A. *Prototype*

The final prototype is presented in Fig. 20 with its most important parts: complete power stage, three-phase transformer, three-phase inductor, the auxiliary supplies for the drivers and the signal isolators, as well as their individual isolated dc–dc converters self-contained into the power stage.

Transistor selection for the first generation of the prototype is, for the high-voltage side inverter, GS66508T from GaN Systems (650-V, 30-A, 50-mΩ GaN E-HEMT) and, for the rectifier, BSZ018N04LS6 from Infineon (40-V, 158-A, 1.8-mΩ Si MOSFET).

B. *Transformer*

The connection of the primary is trivial as there is no track entanglement in the PCB. Fig. 21 represents two possible solutions when creating the delta connection in the secondary of the transformer. Depending on the connection, the rectifier will lag the inverter by 30° or lead it by 30° (Yd11).

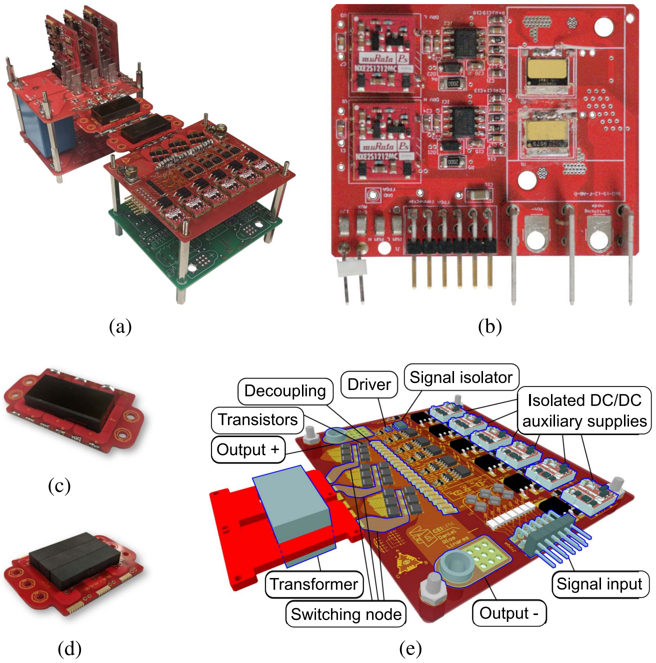

Fig. 20. Prototype key parts. (a) Power stage. (b) Inverter card. (c) Transformer. (d) Inductor. (e) Rectifier composition.

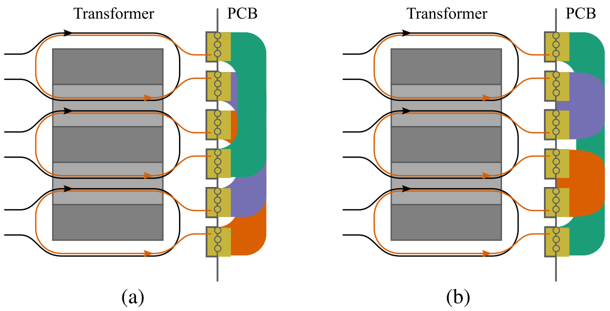

Fig. 21. Delta connection on the secondary (Yd1/Yd11). (a) Proposed connection (Yd1). (b) Alternative connection (Yd11).

Both solutions are correct implementations of the topology. They differ in the PCB layout execution (Fig. 22(a) is the most symmetric) and the modulation in the form of a delay.

VI. EXPERIMENTAL RESULTS

A. *Operation of the Converter*

For aircraft applications, heat is extracted via an isothermal baseplate at constant temperature (90 °C) integrated in a metal housing. As these conditions were not possible to replicate in the laboratory, it was tested with forced air convection at ambient temperature instead.

Fig. 22 shows the experimental waveforms of the converter for $f_S = 900$ kHz, including the drain–source voltage of the low-side transistors for each phase of the inverter [see Fig. 23(a)] and the rectifier [see Fig. 23(c)], as well as current waveforms through each resonant tank [see Fig. 23(b)].

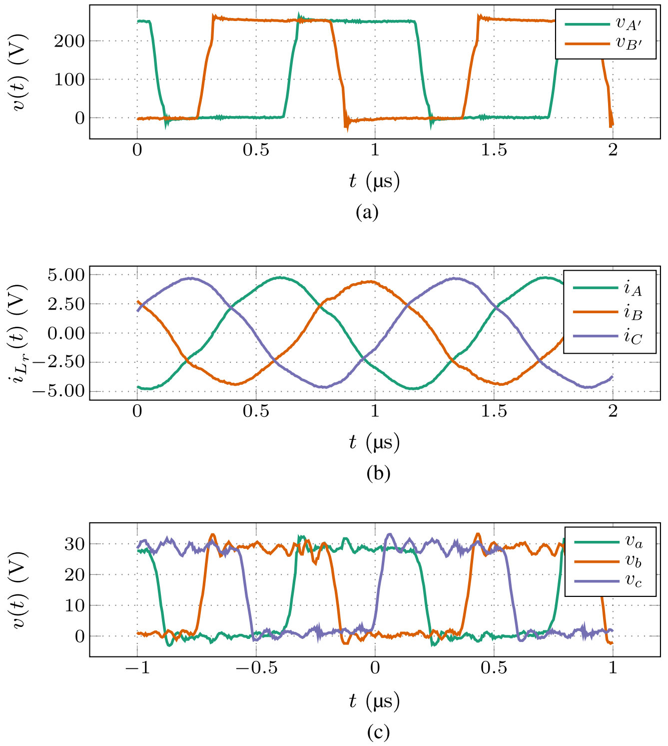

Fig. 22. Experimental waveforms for 250 to 28 V at 1 kW. (a) Voltage at the switching nodes (resonant tank terminals). (b) Currents through the resonant tanks. (c) Voltage at the switching nodes (delta terminals).

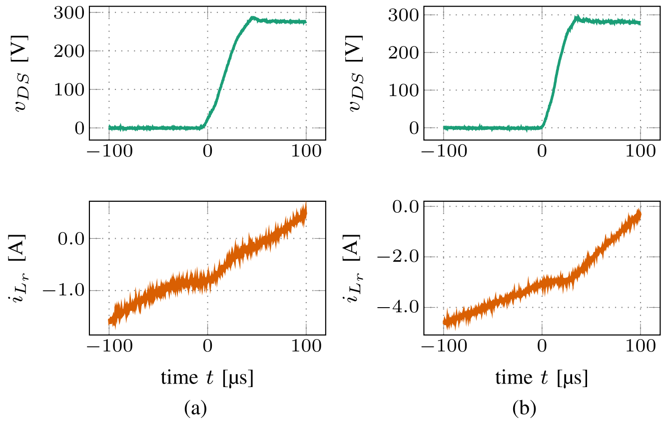

Fig. 23. Inverter voltage ZVS transition at $V_I = 270$ V. (a) $P_O = 100$ W. (b) $P_O = 1000$ W.

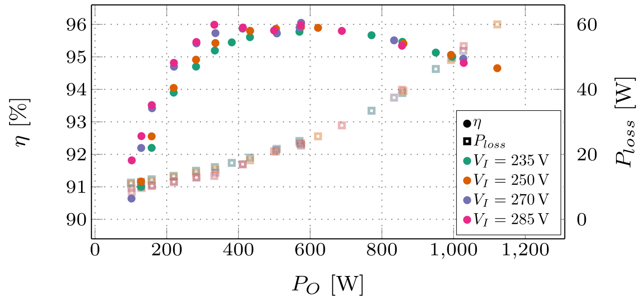

Fig. 24. Measured efficiency for 235–285 V of input voltage and the 100–1000 W output power range.

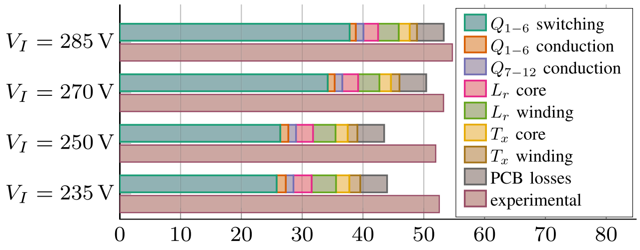

Fig. 25. Theoretical power loss breakdown comparison with experimental at $P_O = 1$ kW.

Fig. 23 illustrates the dynamic ZVS transition characteristics experimentally, presenting the drain–source voltage and switching current for the full output power range (100 and 1000 W).

The tests were not performed acting on the switching current, but by keeping the output voltage constant in an open-loop manner. The observed difference in switching currents between the two cases is attributed to the converter operating above resonance. While a higher switching frequency is necessary for lower power levels (see Fig. 8) and hence increasing the inductive energy, higher load currents require the converter to adapt by adjusting the timing of the switching events (inverter–rectifier delay), resulting in proportionally higher currents during the switching as the output power increases.

The effect of this off-current level is very subtle in switching losses, as demonstrated in [32].

B. Efficiency of the Converter

The efficiency reached by this converter is over 95% in the 333–1000 W output power range for the entire input voltage range with a maximum of 96% at 580 W, as shown in Fig. 24.

All the experiments were made in an open-loop manner and tuning the frequency manually to obtain 28 V at the output (±1%) with the input voltage constant within a 2% of absolute maximum deviation.

The tests revealed a ±11% of frequency variation for the ±15% target, operating in the range 0.93–1.17 MHz.

Fig. 25 shows a theoretical breakdown of power losses at full load across the full range of input voltage levels (235–285 V) compared with experimental measurements. Conduction losses were calculated with the data provided by the manufacturer (ON-resistance at the junction temperature), while switching losses were obtained with the model and data in [32] for the inverter transistors Q_1–Q_6. As Q_7–Q_{12} are operated in ZCS, no voltage and current overlap losses are added due to switching.

The most significant source of power losses is the inverter transistor; even though ZVS is present in the entire load range ($E_{\text{on}} = 0$ µJ), as shown in Fig. 24, switching energy loss cannot be completely eliminated (E_{off}). This is because the transistor channel needs to be shut down as there will be simultaneous current and voltage across it during the transient.

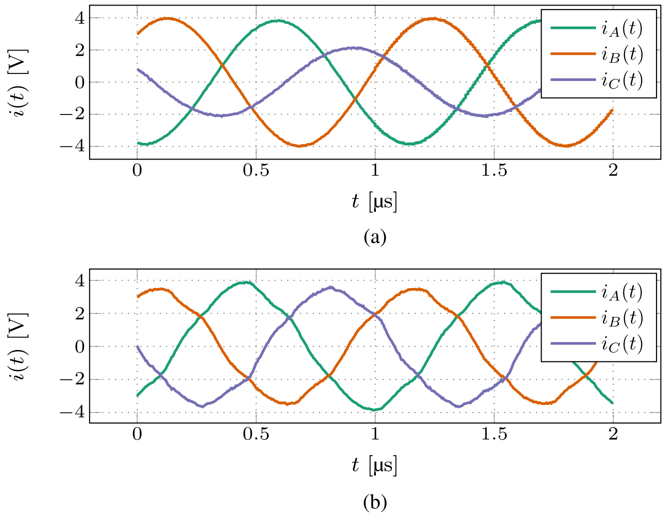

Fig. 26. Experimental waveforms for inductor currents for different inductors (compensated and uncompensated). (a) Uncompensated inductor and transformer with the three legs equal ($|\Delta M/M| < 17\%$). (b) Compensated inductor and transformer manufactured according to Table IV ($|\Delta M/M| < 5\%$).

Power losses for magnetic components have been obtained from electromagnetic simulations and core loss measurements for trapezoidal B-field waveforms, as explained in Section IV.

C. Effect of the Uncompensated Magnetic Core

With the help of an impedance analyzer and for the ML91S material from Proterial, the **Z** matrix was measured for both the transformer and the inductor obtaining an error not greater than 5%, with the sensitivity of μ_c of the material and the tolerance of the air gap being the sources subject to the most uncertainty.

The experimental inductance matrices according to (29a) for the transformer and (36) for the inductor are shown in (42) and (43), respectively:

$$\mathbf{L}_{T_x} = \begin{bmatrix} 12.90 & 2.56 & 7.00 & -1.44 & 5.16 & -1.07 \\ 2.55 & 0.52 & -1.43 & 0.29 & -1.06 & 0.22 \\ 7.00 & -1.43 & 14.56 & 2.88 & 6.80 & -1.40 \\ -1.44 & 0.29 & 2.88 & 0.59 & -1.40 & 0.29 \\ 5.15 & -1.06 & 6.80 & -1.40 & 12.68 & 2.50 \\ -1.07 & 0.22 & -1.40 & 0.28 & 2.50 & 0.51 \end{bmatrix} \ \mu\text{H} \tag{42}$$

$$\mathbf{L}_{L_r} = \begin{bmatrix} 5.85 & 2.50 & 2.31 \\ 2.49 & 5.81 & 2.53 \\ 2.31 & 2.53 & 5.93 \end{bmatrix} \ \mu\text{H}. \tag{43}$$

In the analysis conducted in Section III-A, a coupling factor of $k = 1$ was initially assumed. Based on the data in (42) and the single-phase equivalent described in (28), the coupling factor measured exceeds $k = 0.98$, thus validating the correctness of the initial assumption.

The most undesirable effect is given by the inductor L_r due to series coupling when unbalanced. For this purpose, its error is calculated as the relative error of the main diagonal and the mutuals separately from (43)

$$\text{error} = \begin{bmatrix} -0.23\,\% & 2.20\,\% & -5.84\,\% \\ 1.81\,\% & -0.92\,\% & 3.36\,\% \\ -5.84\,\% & 3.36\,\% & 1.12\,\% \end{bmatrix}. \tag{44}$$

The overall magnitude error when comparing it with the simulated and calculated errors is 12% lower, increasing the resonant frequency by 6%. The reason is given by numerous effects such as unavoidable air gap, air-gap resolution, manufacturing tolerances in manufacturing, and uncertainty in the permeability of the material.

Fig. 26 represents the effect of the compensation of the geometry to obtain a three-phase balanced system, showing once again that in the case of three-phase magnetics, the central leg must be tuned according to (23), and finally evaluating (38b) and (34b) to obtain the desired equivalent inductances (resonant and magnetizing, respectively).

VII. CONCLUSION

In this article, a dc–dc converter was designed, validated, and built to fulfill the strict demands of aircraft applications. A wide input voltage (235–285 V) and high frequency (1 MHz) with a narrow operating frequency span (0.93–1.17 MHz) achieving ±11% in normal operation and with an output power of 1 kW.

Given that the nominal output voltage is 28 V, a high-voltage step-down was required for which a three-phase LLC was proposed to lessen the RMS current per device and open up the design to three-phase transformers. In particular, the wye–delta configuration is the one that minimizes the number of turns of the primary leading to a smaller window and enabling the use of PCB windings.

The method of resonant inductors in a three-phase inductor (and a single three-phase transformer) enables the use of 65% less copper (due to a reduced number of turns) and 60% less ferrite (utilizing a single magnetic core) while maintaining the same specifications.

The main nonidealities of magnetic components were addressed, including equivalent path length, fringing effect, as well as its effect on different winding strategies in terms of losses. The reluctance model of EE and EI cores was derived, quantified via finite-element simulation, and experimentally demonstrated with a 5% error allowing ZVS in the entire load range.

The system was tested for the entire input voltage range (235–285 V) and the output voltage range (100–1000 W) obtaining a 96% maximum efficiency (power losses under 50 W).

With all the critical design features identified, a validated concept, accurate models, and a working prototype, a smart optimization at system and component levels can be performed. Guidelines to model and design the system are yet to be listed and analyzed in depth in future research work.

APPENDIX A
RELUCTANCE MODEL OF AN EE CORE

A significant aspect that requires careful consideration is the design of magnetic core structure. In particular, the transformer

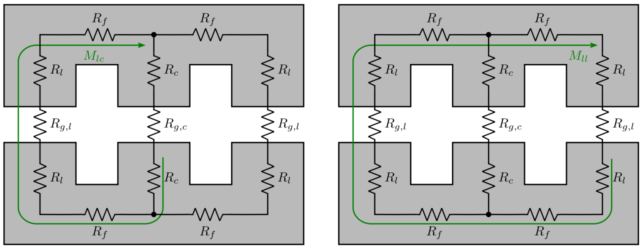

(a) (b)

Fig. 27. Reluctance model. (a) M_{lc} calculation. (b) M_{ll} calculation.

employs a nonsymmetrical configuration with three independent magnetic paths corresponding to the three columns.

To this end, and to complement the magnetostatic model detailed in Section III-A, a reluctance model is employed to equalize the mutual inductances between columns. By analyzing the magnetic flux distribution, a compensation technique is introduced. This compensation involves narrowing the central column while having two identical lateral columns, effectively altering the magnetic paths to achieve balanced coupling.

As a result, the equivalent reluctance model ensures that mutual inductances become equivalent in lateral-to-central and lateral-to-lateral loops, obtaining a balanced interaction between the phases. This optimized configuration leads to reduced power losses, improved thermal stability, and enhanced overall efficiency of the three-phase LLC resonant converter.

In this regard, Hopkinson's law is applied for every section of the magnetic core

$$R_f = \frac{l_a}{\mu_0 \mu_r A_f} \tag{45a}$$

$$R_l = \frac{l_b}{\mu_0 \mu_r A_l},\ R_c = \frac{l_b}{\mu_0 \mu_r A_c} \tag{45b}$$

$$R_{g,l} = \frac{l_g}{\mu_0 \sigma_l A_l},\ R_{g,c} = \frac{l_g}{\mu_0 \sigma_c A_c}. \tag{45c}$$

To have $M_{lc} \equiv M_{ll}$, the sum of reluctances along magnetic paths drawn in green in Fig. 27 must be equal

$$2R_c + R_{g,c} = 2R_f + 2R_l + R_{g,l} \tag{46}$$

resulting in the same expression as in (23)

$$A_l^* = A_c \cdot \frac{A_f \left(2\dfrac{l_b}{\mu_c} + \dfrac{l_g}{\sigma_l}\right)}{A_f \left(2\dfrac{l_b}{\mu_c} + \dfrac{l_g}{\sigma_c}\right) - 2A_c \dfrac{l_a}{\mu_c}}. \tag{47}$$

ACKNOWLEDGMENT

The authors would like to gratefully acknowledge Hitachi Metals for their invaluable contribution to this research for providing high-quality ferrite cores that played a crucial role in the experimental work presented in this article. The authors extend their appreciation for their commitment to scientific progress and technological innovation. The authors would like to especially thank the Princeton University Team, in particular Diego Serrano López who made the measurements, that allowed them to test their magnetic components.

REFERENCES

[1] M. Tariq, A. I. Maswood, C. J. Gajanayake, and A. K. Gupta, "Modeling and integration of a lithium-ion battery energy storage system with the more electric aircraft 270 V DC power distribution architecture," *IEEE Access*, vol. 6, pp. 41785–41802, 2018.

[2] B.-R. Lin and H.-Y. Shih, "ZVS converter with parallel connection in primary side and series connection in secondary side," *IEEE Trans. Ind. Electron.*, vol. 58, no. 4, pp. 1251–1258, Apr. 2011.

[3] B.-R. Lin and J.-Y. Dong, "ZVS resonant converter with parallel-series transformer connection," *IEEE Trans. Ind. Electron.*, vol. 58, no. 7, pp. 2972–2979, Jul. 2011.

[4] B.-R. Lin and S.-F. Wu, "ZVS resonant converter with series-connected transformers," *IEEE Trans. Ind. Electron.*, vol. 58, no. 8, pp. 3547–3554, Aug. 2011.

[5] A. de Juan, D. Serrano, P. Alou, J.-N. Mamousse, R. Deniéport, and M. Vasic, "High-frequency LLC converter with narrow frequency variations for aircraft applications," in *Proc. IEEE Appl. Power Electron. Conf. Expo.*, 2022, pp. 2098–2105.

[6] S. Iqbal, "Interleaved LLC resonant converter with integrated dual transformer for PV power systems," in *Proc. 8th IET Int. Conf. Power Electron., Mach. Drives*, 2016, pp. 1–6.

[7] G. Li and X. Wu, "A 98.4% 380V-12V DCX with 1.3 kW/in^3 power density using low NFoM devices and resonant drive transformer," *IEEE Trans. Power Electron.*, vol. 37, no. 10, pp. 12346–12356, Oct. 2022.

[8] G. C. Knabben et al., "Conceptualization and analysis of a next-generation ultra-compact 1.5-kW PCB-integrated wide-input-voltage-range 12V-output industrial DC/DC converter module," *Electronics*, vol. 10, no. 17, 2021, Art. no. 2158.

[9] R. Ren, B. Liu, E. A. Jones, F. F. Wang, Z. Zhang, and D. Costinett, "Capacitor-clamped, three-level GaN-based DC–DC converter with dual voltage outputs for battery charger applications," *IEEE Trans. Emerg. Sel. Topics Power Electron.*, vol. 4, no. 3, pp. 841–853, Sep. 2016.

[10] T. Jiang, J. Zhang, X. Wu, K. Sheng, and Y. Wang, "A bidirectional three-level LLC resonant converter with PWAM control," *IEEE Trans. Power Electron.*, vol. 31, no. 3, pp. 2213–2225, Mar. 2016.

[11] J.-Y. Lin, H.-Y. Yueh, Y.-F. Lin, and P.-H. Liu, "Analysis and design of three-phase LLC resonant converter with matrix transformers," *Energies*, vol. 15, 2022, Art. no. 1315.

[12] E. Orietti, P. Mattavelli, G. Spiazzi, C. Adragna, and G. Gattavari, "Current sharing in three-phase LLC interleaved resonant converter," in *Proc. IEEE Energy Convers. Congr. Expo.*, 2009, pp. 1145–1152.

[13] Y. Li, S. Shao, H. Chen, J. Zhang, and K. Sheng, "High-gain high-efficiency IPOS LLC converter with coupled transformer and current sharing capability," *CPSS Trans. Power Electron. Appl.*, vol. 5, no. 1, pp. 63–73, Mar. 2020.

[14] R. Gadelrab, A. Nabih, F. C. Lee, and Q. Li, "LLC resonant converter with 99% efficiency for data center server," in *Proc. IEEE Appl. Power Electron. Conf. Expo.*, 2021, pp. 310–319.

[15] C. Fei, R. Gadelrab, Q. Li, and F. C. Lee, "High-frequency three-phase interleaved LLC resonant converter with GaN devices and integrated planar magnetics," *IEEE Trans. Emerg. Sel. Topics Power Electron.*, vol. 7, no. 2, pp. 653–663, Jun. 2019.

[16] R. Mirzahosseini and F. Tahami, "A phase-shift three-phase bidirectional series resonant DC/DC converter," in *Proc. 37th Annu. Conf. IEEE Ind. Electron. Soc.*, 2011, pp. 1137–1143.

[17] R. Gadelrab and F. C. Lee, "PCB-based magnetic integration and design optimization for three-phase LLC," *IEEE Trans. Power Electron.*, vol. 38, no. 11, pp. 14037–14049, Nov. 2023.

[18] H. Matsumori, T. Shimizy, K. Takano, and H. Ishii, "Three-phase AC filter inductor design for three-phase PWM inverter for conversion efficiency improvement at low load," *Elect. Eng. Jpn.*, vol. 203, no. 1, pp. 37–49, 2018.

[19] M. Noah et al., "Magnetic design and experimental evaluation of a commercially available single integrated transformer in three-phase LLC resonant converter," *IEEE Trans. Ind. Appl.*, vol. 54, no. 6, pp. 6190–6204, Nov./Dec. 2018.

[20] A. Anurag, S. Acharya, S. Bhattacharya, T. R. Weatherford, and A. A. Parker, "A Gen-3 10-kV SiC MOSFET-based medium-voltage three-phase dual active bridge converter enabling a mobile utility support equipment solid state transformer," *IEEE Trans. Emerg. Sel. Topics Power Electron.*, vol. 10, no. 2, pp. 1519–1536, Apr. 2022.

[21] A. de Juan, D. Serrano, P. Alou, J.-N. Mamousse, R. Denéieport, and M. Vasic, "Analytical modelling of single-phase and three-phase DC/DC LLC converters," in *Proc. IEEE Appl. Power Electron. Conf. Expo.*, 2022, pp. 2106–2113.

[22] X. Fang, H. Hu, Z. J. Shen, and I. Batarseh, "Operation mode analysis and peak gain approximation of the LLC resonant converter," *IEEE Trans. Power Electron.*, vol. 27, no. 4, pp. 1985–1995, Apr. 2012.

[23] V. S. Duppalli and S. Sudhoff, "Power density comparison of three-phase AC inductor architectures," in *Proc. IEEE Electr. Ship Technol. Symp.*, 2017, pp. 217–224.

[24] A. Balakrishnan, W. Joines, and T. Wilson, "Air-gap reluctance and inductance calculations for magnetic circuits using a Schwarz-Christoffel transformation," *IEEE Trans. Power Electron.*, vol. 12, no. 4, pp. 654–663, Jul. 1997.

[25] J. Muhlethaler, J. W. Kolar, and A. Ecklebe, "A novel approach for 3D air gap reluctance calculations," in *Proc. 8th Int. Conf. Power Electron.*, 2011, pp. 446–452.

[26] H. Li, S. R. Lee, M. Luo, C. R. Sullivan, Y. Chen, and M. Chen, "MagNet: A machine learning framework for magnetic core loss modeling," in *Proc. IEEE 21st Workshop Control Model. Power Electron.*, 2020, pp. 1–8.

[27] J. Schäfer, D. Bortis, and J. W. Kolar, "Novel highly efficient/compact automotive PCB winding inductors based on the compensating air-gap fringing field concept," *IEEE Trans. Power Electron.*, vol. 35, no. 9, pp. 9617–9631, Sep. 2020.

[28] M. K. Ranjram, P. Acosta, and D. J. Perreault, "Design considerations for planar magnetic terminations," in *Proc. 20th Workshop Control Model. Power Electron.*, 2019, pp. 1–8.

[29] M. Kazimierczuk, *High-Frequency Magnetic Components*, 2nd ed. Hoboken, NJ, USA: Wiley, 2013.

[30] R. Shafaei, M. C. G. Perez, and M. Ordonez, "Planar transformers in LLC resonant converters: High-frequency fringing losses modeling," *IEEE Trans. Power Electron.*, vol. 35, no. 9, pp. 9632–9649, Sep. 2020.

[31] Y. Cao, M. Ngo, N. Yan, D. Dong, R. Burgos, and A. Ismail, "Design and implementation of an 18-kW 500-kHz 98.8% efficiency high-density battery charger with partial power processing," *IEEE Trans. Emerg. Sel. Topics Power Electron.*, vol. 10, no. 6, pp. 7963–7975, Dec. 2022.

[32] E. A. Jones et al., "Characterization of an enhancement-mode 650-V GaN HFET," in *Proc. IEEE Energy Convers. Congr. Expo.*, 2015, pp. 400–407.

Daniel Ríos Linares (Student Member, IEEE) received the B.Sc. degree in industrial electronics engineering from the University of Granada, Granada, Spain, in 2019, and the M.Sc. degree in industrial electronics engineering from the Universidad Politécnica de Madrid, Madrid, Spain, where he is currently working toward the Ph.D. degree with the Centro de Electrónica Industrial, in 2021.

His research interests include design of dc–dc power converters, topologies, and optimization of high-frequency applications.

Alberto Delgado Expósito (Member, IEEE) received the B.Sc. degree in electrical engineering from the University of Malaga, Malaga, Spain, in 2016, and the M.Sc. and Ph.D. degrees in industrial electronics from the Universidad Politécnica de Madrid (UPM), Madrid, Spain, in 2017 and 2021, respectively.

He became a Teaching Assistant with UPM in 2019. His research interests include modeling of dc–dc converters for inductive power transfer systems and magnetic components for different applications, such as radio frequency identification communications and wireless charging and magnetic nanomaterials and micromaterials.

Dr. Expósito was a recipient of the Best Student of the Year Award and honors on several occasions, during his undergraduate studies.

Miroslav Vasić (Senior Member, IEEE) was born in Serbia, in 1981. He received the B.S. degree in electrical engineering from the School of Electrical Engineering, University of Belgrade, Belgrade, Serbia, in 2005, and the M.S. and Ph.D. degrees in industrial electronics from the Centro de Electronica Industrial, Escuela Tecnica Superior de Ingenieros Industriales (ETSII), Universidad Politécnica de Madrid (UPM), Madrid, Spain, in 2007 and 2010, respectively.

He has been an Associate Professor with the Centro de Electronica Industrial, ETSII, UPM, since 2019. In recent years, a great part of his research activities has been related to the research of new semiconductor devices based on gallium nitride and their impact on power electronics. He has authored or coauthored more than 70 peer-reviewed technical papers at conferences and in IEEE journals, and he advised five Ph.D. theses and holds six patents. His research interests include the application of power converters and their optimization.

Dr. Vasić was a recipient of the Semikron Innovation Award for the teamwork on "RF Power Amplifier With Increased Efficiency and Bandwidth" in 2012, a medal from the Spanish Royal Academy of Engineering as a recognition of his research trajectory in 2015, and the UPM Research Projection Award for the Best Young Researcher at UPM in 2016. He is an Associate Editor for IEEE JOURNAL OF EMERGING AND SELECTED TOPICS IN POWER ELECTRONICS and IEEE TRANSACTIONS ON VEHICULAR TECHNOLOGY. He was one of the cofounders of the Technical Committee on Design Methodologies of IEEE Power Electronics Society and acted as the Vice-Chair from 2021 to 2023.